Geophysical Journal International

Geophys. J. Int. (2017) **211,** 1461–1477
Advance Access publication 2017 September 13
GJI Geomagnetism, rock magnetism and palaeomagnetism

doi: 10.1093/gji/ggx381

LCS-1: a high-resolution global model of the lithospheric magnetic field derived from CHAMP and *Swarm* satellite observations

Nils Olsen,[1] Dhananjay Ravat,[2] Christopher C. Finlay[1] and Livia K. Kother[1]

[1] *DTU Space, National Space Institute, Technical University of Denmark, Diplomvej* 371, 2800 *Kgs. Lyngby, Denmark. E-mail: nio@space.dtu.dk*
[2] *Department of Earth and Environmental Sciences, University of Kentucky, Kentucky* 40506, *USA*

Accepted 2017 September 10. Received 2017 September 8; in original form 2017 May 25

SUMMARY

We derive a new model, named LCS-1, of Earth's lithospheric field based on four years (2006 September–2010 September) of magnetic observations taken by the CHAMP satellite at altitudes lower than 350 km, as well as almost three years (2014 April–2016 December) of measurements taken by the two lower *Swarm* satellites Alpha and Charlie. The model is determined entirely from magnetic 'gradient' data (approximated by finite differences): the north–south gradient is approximated by first differences of 15 s along-track data (for CHAMP and each of the two *Swarm* satellites), while the east–west gradient is approximated by the difference between observations taken by *Swarm Alpha* and *Charlie*. In total, we used 6.2 mio data points. The model is parametrized by 35 000 equivalent point sources located on an almost equal-area grid at a depth of 100 km below the surface (WGS84 ellipsoid). The amplitudes of these point sources are determined by minimizing the misfit to the magnetic satellite 'gradient' data together with the global average of $|B_r|$ at the ellipsoid surface (i.e. applying an L1 model regularization of B_r). In a final step, we transform the point-source representation to a spherical harmonic expansion. The model shows very good agreement with previous satellite-derived lithospheric field models at low degree (degree correlation above 0.8 for degrees $n \leq 133$). Comparison with independent near-surface aeromagnetic data from Australia yields good agreement (coherence >0.55) at horizontal wavelengths down to at least 250 km, corresponding to spherical harmonic degree $n \approx 160$. The LCS-1 vertical component and field intensity anomaly maps at Earth's surface show similar features to those exhibited by the WDMAM2 and EMM2015 lithospheric field models truncated at degree 185 in regions where they include near-surface data and provide unprecedented detail where they do not. Example regions of improvement include the Bangui anomaly region in central Africa, the west African cratons, the East African Rift region, the Bay of Bengal, the southern 90°E ridge, the Cretaceous quiet zone south of the Walvis Ridge and the younger parts of the South Atlantic.

Key words: Composition and structure of the continental crust; Composition and structure of the oceanic crust; Magnetic anomalies: modelling and interpretation; Satellite magnetics; Inverse theory; Spatial analysis.

1 INTRODUCTION

Determination of global lithospheric field models requires accurate magnetic field observations with global coverage, which can only be obtained by satellites. Consequently, the construction of lithospheric magnetic field models is one of the main objectives of satellite missions such as CHAMP and *Swarm*. During the past decade, a number of global lithospheric field models have been determined from data collected by these satellites (e.g. Thébault *et al.* 2017). In one class of models, the lithospheric field is co-estimated together with other magnetic sources (e.g. from the core and magnetosphere) in a comprehensive approach; such models include the comprehensive model (CM) series (e.g. Sabaka *et al.* 2004, 2015), the GRIMM models (e.g. Lesur *et al.* 2008, 2015), the BGS model series (e.g. Thomson & Lesur 2007; Thomson *et al.* 2010) and the CHAOS model series (e.g. Olsen *et al.* 2014; Finlay *et al.* 2016). Models of the other class are derived in a sequential approach by first removing *a priori* models of all known magnetic field contributions, except for the lithospheric field, from the magnetic field observations, followed by a careful data selection and application of empirical corrections. The MF model series (e.g. Maus *et al.* 2002, 2008; Maus 2010) are examples of models determined using this approach; other

© The Authors 2017. Published by Oxford University Press on behalf of The Royal Astronomical Society.

examples are the models determined by Stockmann *et al.* (2009), Kother *et al.* (2015) and Thébault *et al.* (2016).

The MF7 model developed by Maus and co-workers is one of the most widely used global lithospheric field models. It formally describes the lithospheric field up to spherical harmonic degree $n = 133$ (corresponding to 300 km horizontal wavelength), and has been derived from along-track filtered CHAMP magnetic field observations after removal of *a priori* models of the core and large-scale magnetospheric fields and of the ocean tidal magnetic signal, and line leveling between adjacent satellite tracks and nearby orbit crossovers to minimize the variance between observations within a certain distance. Coefficients above $n > 80$ are damped (regularized) by minimizing the L2 norm of the radial magnetic field, which means minimizing B_r^2 averaged over the Earth's surface.

As an alternative to the L2 norm of B_r, other regularization schemes have also been used: Stockmann *et al.* (2009) and Kother *et al.* (2015) applied a maximum entropy regularization (of B_r and equivalent source amplitudes respectively), while Morschhauser *et al.* (2014) used an L1 model regularization of B_r, which means minimizing $|B_r|$ averaged over the surface of interest, for modeling the lithospheric field of Mars.

Lithospheric field models differ also in their model parametrization. While most models (including MF7) estimate the coefficients of a spherical harmonic expansion of the magnetic potential, alternatives have been explored. These include spherical triangle tessellations of B_r (Stockmann *et al.* 2009), (depleted) harmonic splines (Langel & Whaler 1996), equivalent dipole sources (e.g. Mayhew 1979; von Frese *et al.* 1981; Dyment & Arkani-Hamed 1998), spherical caps (e.g. Haines 1985; Thébault 2006, 2008) and an equivalent source method involving monopoles (O'Brien & Parker 1994; Kother *et al.* 2015).

In this paper, we present a new global model of the lithospheric field that has been derived using more satellite magnetic observations (utilizing four years of data from CHAMP and three years from *Swarm*) than in previous models, using an equivalent source model parametrization consisting of 35 000 point sources (monopoles), and using an L1 norm model regularization that minimizes the global average of $|B_r|$ at the ellipsoid. Use of L1 norm model regularization in the construction of lithospheric field models is motivated by the lithospheric field being characterized by a small number of localized high-amplitude continental features, together with generally low-amplitude features in the extended oceanic regions.

Due to its quadratic form, the L2 norm is dominated by the contribution from high-amplitude features. Minimizing the L2 norm therefore suppresses such high-amplitude features, while having relatively little impact on possibly spurious features in low-amplitude regions. In contrast, the L1 norm penalizes in a similar way unneeded signal in both low- and high-amplitude regions.

Therefore, compared to an L2 norm regularized model with a similar misfit, an L1 norm regularized model will possess locally higher amplitude features where needed, and at the same time, it will suppress more efficiently unneeded signals in low-amplitude regions. This permits models described as 'sparse' (e.g. Aster *et al.* 2013, section 7.2) in the sense that much of the model can be close to zero, while at the same time there can be a small number of high-amplitude features, which is in agreement with our expectations for a model of the lithospheric field.

Low-altitude magnetic field measurements are crucial for constructing high-quality lithospheric field models, due to the comparatively rapid attenuation of the lithospheric signal with altitude. This is obvious from Fig. 1 which shows the *Lowes–Mauersberger* spatial spectrum of the lithospheric field at various altitudes as given by the MF7 lithospheric model (Maus 2010).

At Earth's surface, the spectrum is essentially 'flat' (i.e. independent of n) in the presented wavelength range ($\lambda = 300$–2500 km), whereas it strongly decreases with increasing harmonic degree n at satellite altitude. Focusing, for example, on lithospheric structures with horizontal wavelength $\lambda = 400$ km (corresponding to spherical harmonic degree $n = 100$), the mean lithospheric amplitude when averaging over Earth's surface is about 7 nT, whereas it is only 56 pT at 300 km altitude, which was the altitude of the CHAMP satellite during the last few months of the mission. At 450 km altitude, which is the present altitude of the lower *Swarm* satellite pair, the lithospheric signal is only 5.8 pT, 10 times weaker than at 300 km altitude. The attenuation with altitude is even stronger at higher spherical harmonic degrees.

Extracting the weak lithospheric signal from the satellite magnetic field observations is thus a major challenge which requires sophisticated statistical methods and data processing schemes. Spatial gradient information on the magnetic field, approximated by finite differences of measurements taken at nearby locations, help in removing the large-scale magnetic field contributions from the core and magnetosphere (and residuals of these effects in the data), and enhance the lithospheric signal. The lithospheric model that we present here relies entirely on such gradient information. We denote our new model as LCS-1 (**L**ithospheric model derived from **C**HAMP and **S***warm* satellite data, version **1**).

Section 2 describes the data set that was used to derive and assess the lithospheric field model, and Section 3 presents how the model is parametrized and estimated. Results are discussed in Section 4, which also includes an investigation of the information content of the different data sets, thereby providing an assessment of the contribution of *Swarm* satellite data to the model. A discussion of the new lithospheric model is given in Section 5. The paper concludes with a summary and outlook in Section 6.

2 DATA

We use magnetic observations collected by the CHAMP and *Swarm* satellite missions. CHAMP (e.g. Maus 2007) was launched in 2000 July into a near-polar (inclination 87.2°) orbit with an initial altitude of 454 km above a mean radius of $a = 6371.2$ km and had its atmospheric re-entry in 2010 September. Altitude during the last four years of the mission was 350 km or lower, which makes this data set particularly interesting for lithospheric field modeling.

The satellite constellation mission *Swarm* (e.g. Friis-Christensen *et al.* 2006; Olsen *et al.* 2016b) was launched in 2013 November. It consists of three identical spacecraft, two of which, *Swarm Alpha* and *Swarm Charlie*, fly closely together in near-polar orbits of inclination 87.4° at an altitude of about 450 km (as of 2017 March). The east–west (EW) separation of their orbits is 1.4° in longitude, corresponding to 155 km at the equator. The third satellite, *Swarm Bravo*, flies at a slightly higher (about 520 km altitude in 2017 March) orbit of inclination 88°. For our modeling effort, we only use data from the two lower satellites *Swarm Alpha* and *Charlie*.

We selected CHAMP data from the four years 2006 September to 2010 September and from the lower *Swarm* satellite pair between 2014 April (since then the two lower satellites are flying in constellation) and 2016 December. The top panel of Fig. 2 shows mean altitude (red curve) and altitude range (red shaded) of the satellites together with solar flux $F_{10.7}$ (blue) with respect to time. The sudden increase in CHAMP altitude in 2009 is due to an orbit manoeuvre.

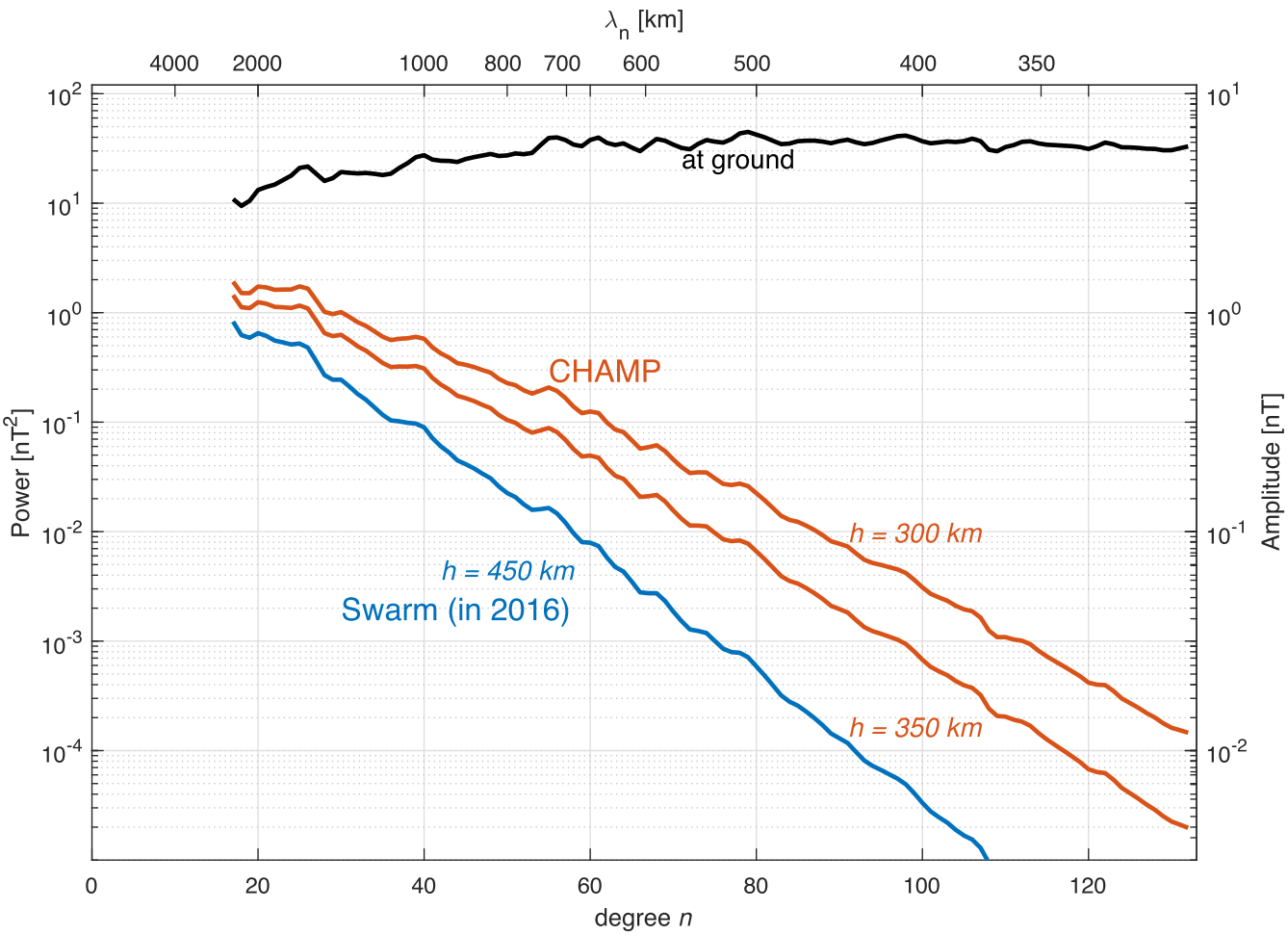

Figure 1. Spatial power spectrum of the lithospheric field at Earth's surface (black curve) and at various altitudes (with respect to a mean geocentric radius of $a = 6371.2$ km) of CHAMP (red) and *Swarm* (blue), as given by the MF7 field model of Maus (2010). λ_n is the horizontal wavelength corresponding to degree n in a spherical harmonic expansion of the field.

Unmodeled large-scale magnetospheric field contributions are one of the largest sources of noise for lithospheric field modeling, and various techniques have been used to eliminate these unwanted features from the data [see Thébault *et al.* (2017) for a recent overview]. Commonly used techniques include high-pass filtering of the satellite magnetic field observations on an orbit-by-orbit basis and line leveling (e.g. Maus 2010). But such pre-processing of the data also removes part of the lithospheric signal, as demonstrated, for example, by Thébault *et al.* (2012).

However, large-scale magnetic field contributions such as those produced by magnetospheric currents are effectively reduced in gradient data compared to the magnetic field itself, which increases the lithospheric signal-to-noise ratio in gradient data. By relying entirely on gradient data, as done here, it is therefore possible to construct lithospheric field models without orbit-by-orbit high-pass filtering or line leveling.

Use of gradient data for lithospheric field modeling has several advantages: (i) since gradient data are less affected by (large-scale) external field contributions, it is possible to include data from times of higher geomagnetic activity, which increases the amount of times with data suitable for lithospheric modeling by up to 50 per cent; (ii) these unmodeled large-scale contributions result in highly correlated satellite field data time-series but much less correlated gradient data time-series. The gradient data are therefore less correlated in time compared to field data, which enables a higher data sampling rate compared to field data. This further increases the amount of useful data for lithospheric field modeling.

In order to estimate our lithospheric model, we rely entirely on horizontal difference data (which we in the following denote as 'gradient data'); we do not use magnetic field observations directly. Note, however, that magnetic field observations are of course used (differenced) when deriving the magnetic gradient data.

2.1 Selection of gradient data for model estimation

We select our data using similar criteria to those used for constructing the CHAOS-6 (Finlay *et al.* 2016) model; however, for the present model we subsampled the nominal 1 Hz data (Level-3 data for CHAMP, and Level-1b version 0501 data for *Swarm*) at 30 s intervals (instead of the 60 s sampling used for CHAOS-6).

Vector and scalar gradient data are selected for periods when (i) the strength of the magnetic signature of the magnetospheric ring current, described using the RC index (Olsen *et al.* 2014), changes by at most 3 nT hr^{-1}; and (b) when the geomagnetic activity index $Kp \leq 3^0$ for quasi-dipole (QD) latitudes (Richmond 1995) equatorward of $\pm 55^\circ$. Vector gradient data are only taken from non-polar (QD latitudes equatorward of $\pm 55^\circ$) regions, while scalar

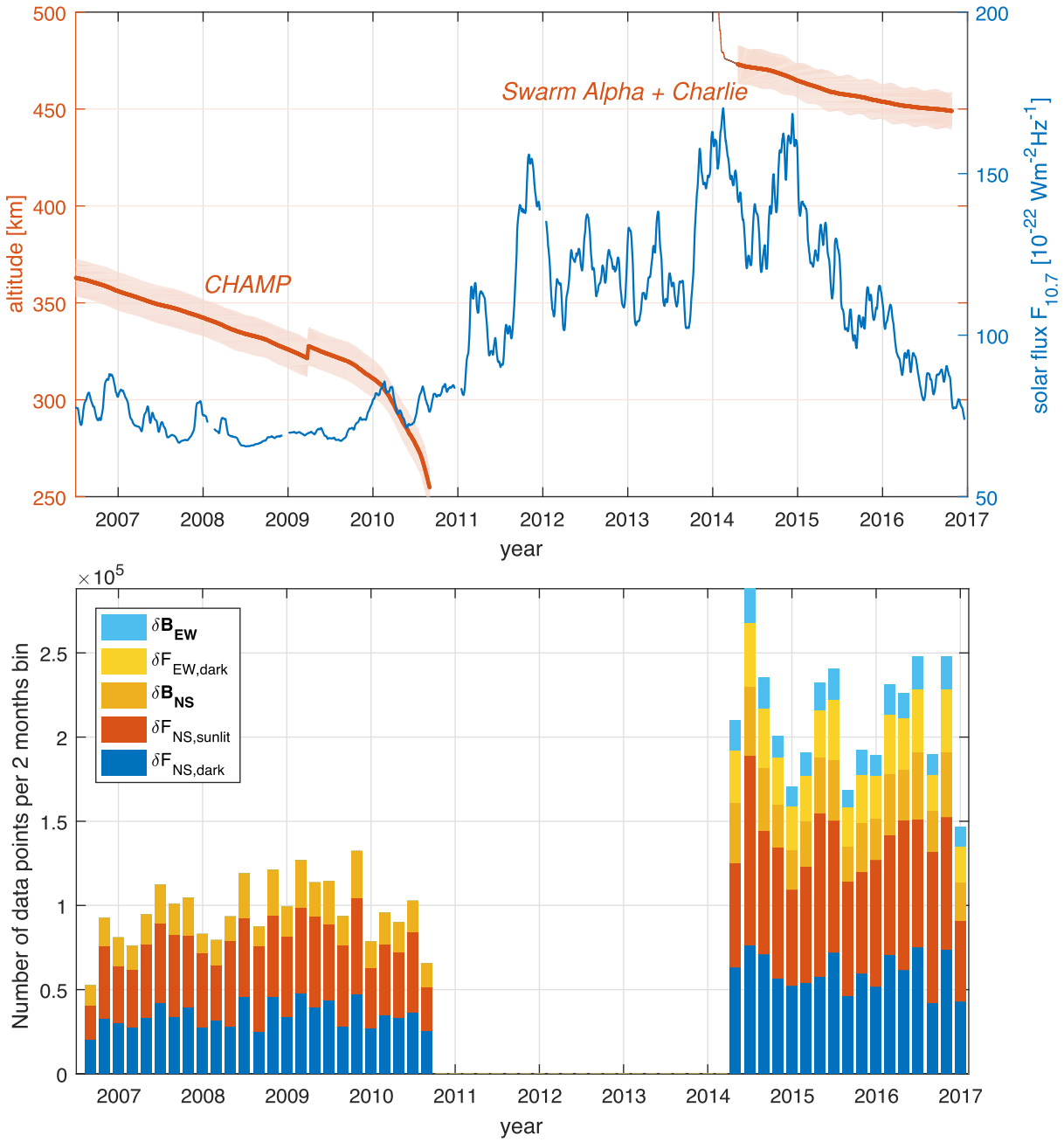

Figure 2. Top: altitude (with respect to a mean geocentric radius of $a = 6371.2$ km) of the CHAMP and *Swarm* satellites (red), and 27 day averages of solar flux index, $F_{10.7}$ (blue). The shaded red regions indicate the altitude range. Bottom: total number of satellite data (stacked histogram) as a function of time, for bins of 2 months length. See the text for details.

gradient data are taken globally. Only data from dark regions (sun at least 10° below the horizon) are chosen with the exception of north–south (NS) scalar gradient data for which we also include data from sunlit (i.e. dayside) regions. However, we do not use any dayside data at QD latitudes $<\pm 10°$ to avoid contamination by the Equatorial Electrojet, following the strategy described by Olsen *et al.* (2015, 2016a).

Similar to CHAOS-6, data in polar regions (poleward of ±55° QD latitude) were selected only when the merging electric field at the magnetopause $E_m \leq 0.8$ mV m^{-1} and when the interplanetary magnetic field was northward directed ($B_Z > 0$).

In order to isolate the lithospheric magnetic signature, we removed from all the magnetic observations predictions of the core field (up to spherical harmonic degree $n = 14$) and of the large-scale magnetospheric field as given by the CHAOS-6_x2 model (which is an extension of the model described in Finlay *et al.* 2016). In the following, we will denote as 'data' these residuals between magnetic observations and CHAOS-6 model predictions.

For each of the three satellites (j denotes CHAMP, *Swarm Alpha* or *Swarm Charlie*), the NS gradient is approximated by the difference $\delta B_{\mathrm{NS}} = B(t_j, r_j, \theta_j, \phi_j) - B(t_j + 15\,\mathrm{s}, r_j + \delta r, \theta_j + \delta\theta, \phi_j + \delta\phi)$ using subsequent data measured by the same satellite 15 s later, corresponding to an along-track distance of ≈115 km (≈1° in latitude). In what follows, B may be either the scalar intensity F or one of the three magnetic vector components (B_r, B_θ, B_ϕ). Here t_j, r_j, θ_j, ϕ_j, are time, radius,

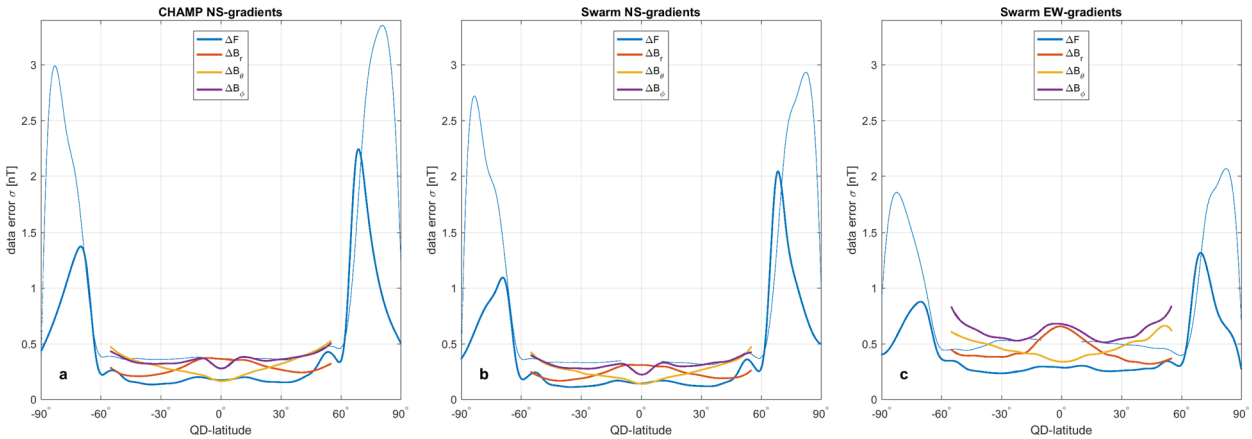

Figure 3. Assigned data uncertainties σ for the CHAMP (left) and *Swarm* (middle and right) satellite gradient data, in dependence on QD latitude. Left: uncertainties of CHAMP along-track 'gradient' (15 s finite difference) data, approximating the north–south gradients δF_{NS}, $\delta \mathbf{B}_{\mathrm{NS}}$. Middle: same, but for *Swarm*. Right: uncertainties of east–west 'gradient' data (difference between observations of *Swarm* Alpha and Charlie) δF_{EW}, $\delta \mathbf{B}_{\mathrm{EW}}$. The thin blue curves represent estimated scalar gradient data uncertainties for sunlit conditions.

geographic co-latitude and longitude of the observation, respectively.

The EW gradient is approximated by the difference $\delta B_{\mathrm{EW}} = B_A(t_1, r_1, \theta_1, \phi_1) - B_C(t_2, r_2, \theta_2, \phi_2)$ of the magnetic observations taken by *Swarm Alpha* and *Charlie*. For each observation B_A (from *Swarm Alpha*) fulfilling the above selection criteria, we selected the corresponding value B_C (from *Swarm Charlie*) that was closest in co-latitude θ, with the additional requirement that the time difference $|\delta t| = |t_1 - t_2|$ between the two measurements should not exceed 50 s.

The bottom panel of Fig. 2 shows the number of data points in bins of 2-months length in time. The amount of *Swarm* data is twice that of the CHAMP data, owing to the availability of EW gradient data which is unique to the *Swarm* constellation mission. In total, we use 5.2 mio NS gradient data δF_{NS}, $\delta \mathbf{B}_{\mathrm{NS}}$ (2.4 mio from CHAMP and 2.8 mio from *Swarm*), and 0.95 mio EW gradient data δF_{EW}, $\delta \mathbf{B}_{\mathrm{EW}}$ (*Swarm* only). This amounts to 6.2 mio data points in total.

We assign to each data point a data uncertainty that depends on QD latitude. These data uncertainties have been determined from the residuals of the data (observations minus core, lithospheric and magnetospheric field contributions) with respect to the CHAOS-6-x2 model by binning the residuals in QD latitudinal bins of 5° width and estimating standard deviation σ using a robust approach (Huber weighting). Fig. 3 shows the assigned data uncertainties for the various data sources and for the CHAMP (left) and *Swarm* (middle and right) satellites.

2.2 Selection of magnetic field data for model assessment

For testing and evaluation purposes, we also selected a data set of magnetic field observations $\mathbf{B}$ and F, again using data selection criteria similar to those used for constructing the CHAOS-6 model (Finlay *et al.* 2016). However, since magnetic field data are more influenced by unmodeled external field contributions compared to gradient data, it is necessary to restrict the selection to periods of lower geomagnetic activity when considering field data compared to gradient data. Following Olsen *et al.* (2015), we take magnetic field data only during extremely quiet conditions when the RC index changes by at most 2 nT hr^{-1} (for gradient data, we allow for changes up to 3 nT hr^{-1}) and when the geomagnetic activity index $Kp \leq 2^0$ (for gradient data, we allow values for $Kp \leq 3^0$). We take vector magnetic field observations only from non-polar latitudes (as we do for gradient data), while only scalar field data are used in the polar regions.

In order to reduce temporal correlation of the data, we downsampled the field values to 2 min. This yields 72 000 polar scalar data (35 500 from CHAMP and 36 500 from *Swarm*) and 250 000 vector triplets (120 000 from CHAMP and 130 000 from *Swarm*). Note that this data set has not been used in the construction of the final LCS-1 lithospheric model.

3 MODEL PARAMETRIZATION AND ESTIMATION

We describe the lithospheric magnetic field $\mathbf{B} = -\nabla V$ using a magnetic scalar potential V of internal origin. Following O'Brien & Parker (1994) and Kother *et al.* (2015), V is modeled as a linear combination of K equivalent potential field sources (monopoles) of amplitudes q_k (given in units of nT), located at the positions $\mathbf{s}_k = [r_k, \theta_k, \phi_k]$, $k = 1, \ldots, K$ where r, θ and ϕ are spherical coordinates. The potential at the position of the N data positions $\mathbf{r}_i = [r_i, \theta_i, \phi_i]$, $i = 1, \ldots, N$ produced by the superposition of the K point sources is

$$V(\mathbf{r}_i) = \sum_{k=1}^{K} q_k \frac{r_k^2}{r_{ik}} \tag{1}$$

where $r_{ik} = |\mathbf{r}_i - \mathbf{s}_k|$ and μ_{ik} are the distance and angle between the position vectors of the observations, $\mathbf{r}_i$, and of the point sources $\mathbf{s}_k$, respectively;

$$r_{ik} = \sqrt{r_i^2 + r_k^2 - 2 r_i r_k \cos(\mu_{ik})} \tag{2a}$$

$$\cos(\mu_{ik}) = \cos(\theta_i)\cos(\theta_k) + \sin(\theta_i)\sin(\theta_k)\cos(\phi_i - \phi_k). \tag{2b}$$

We use $K = 35\,000$ point sources placed horizontally on an approximately equal-area grid defined by the 'Recursive Zonal Equal Area Sphere Partitioning' algorithm of Leopardi (2006). The angular distance d between each point and its nearest neighbours varies between 1.07° and 1.1°, with a median value of 1.088° corresponding to 120.7 km at the Earth's surface. The same value is found

by dividing Earth's surface $4\pi a^2$ (approximated by a sphere of radius a) into K quadratic tesseroids of equal size d^2, which results in $d = a\sqrt{(4\pi/K)} = 120.7$ km. The depth of the point sources is chosen as 100 km below the Earth's surface as given by the World Geodetic System 1984 (WGS84) ellipsoid. This choice of point-source depth is not related to the true depth of lithospheric magnetization, which is likely at much shallower depth. A point source at depth 100 km yields *exactly* the same surface magnetic field as a spatially more extended source distribution at some shallower depth. This is a consequence of the potential nature of the magnetic field. A detailed discussion of numerical considerations related to the choice of equivalent point-source depth is given by O'Brien & Parker (1994).

Collecting the magnetic field observations $(B_{r,i}, B_{\theta,i}, B_{\phi,i})$, $i = 1, \ldots, N$ in the data vector $\mathbf{d_B}$, and the strength of the point sources, q_k, $k = 1, \ldots K$, in the model vector $\mathbf{m}$ results in the linear relationship

$$\mathbf{d_B} = \mathbf{G_B m}\,. \tag{3}$$

The elements of the data kernel matrix $\mathbf{G_B}$ are given in appendix A of Kother *et al.* (2015).

Scalar data (i.e. magnetic field intensity) can be treated by projecting the elements of the kernel matrices $\mathbf{G}_{\mathbf{B},r}$, $\mathbf{G}_{\mathbf{B},\theta}$, $\mathbf{G}_{\mathbf{B},\phi}$ describing the vector field components at data location $\mathbf{r}_i$ on the unit vector $\hat{\mathbf{B}} = \mathbf{B}_{\rm mod}/|\mathbf{B}_{\rm mod}|$ of the ambient core field (given by the CHAOS-6 core field model for spherical harmonic degrees $n = 1$–14) at that location.

Gradient data were handled in a manner similar to that described in Kotsiaros *et al.* (2015) by taking the difference of the kernel matrices $\mathbf{G_B}$ corresponding to the two positions involved in the spatial difference, (r_1, θ_1, ϕ_1) and (r_2, θ_2, ϕ_2).

Collecting the observations of vector gradient $\delta\mathbf{B}$ and scalar gradient δF in the data vector $\mathbf{d}$, we follow Farquharson & Oldenburg (1998) in estimating the model vector $\mathbf{m}$ by minimizing the cost function $\Phi = \Phi_{\rm data} + \alpha^2\Phi_{\rm model}$ consisting of the sum of the data misfit norm $\mathbf{e}^T\mathbf{W}_d\mathbf{e}$ and the model regularization norm $\alpha^2\mathbf{m}^T\mathbf{Rm}$:

$$\Phi = \mathbf{e}^T\mathbf{W}_d\mathbf{e} + \alpha^2\mathbf{m}^T\mathbf{Rm} \tag{4}$$

where $\mathbf{e} = \mathbf{d} - \mathbf{Gm}$ is the data misfit vector (difference between data $\mathbf{d}$ and model predictions $\mathbf{d}_{\rm mod} = \mathbf{Gm}$), $\mathbf{W}_d$ is the diagonal data weight matrix with elements w/σ^2 (where σ^2 are the data variances as shown in Fig. 3 and w are the robust data weights) and $\mathbf{R}$ is a model regularization matrix which results in the minimization of the global average of $|B_r|$ at Earth's surface ellipsoid. The parameter α^2 controls the relative contribution of the model regularization norm to the cost function Φ.

To obtain the model regularization matrix $\mathbf{R}$, we synthesize, for a given model $\mathbf{m}$, the radial magnetic field B_r at 50 000 equally distributed locations on the Earth's surface (ellipsoid, median spacing 100 × 100 km); collecting these values in the vector $\mathbf{b} = \{B_r\}$ allows us to write this transformation in matrix form as $\mathbf{b} = \mathbf{Am}$. The model regularization matrix used in our scheme to implement the L1 norm is updated iteratively as $\mathbf{R} = \mathbf{A}^T\mathbf{W}_m\mathbf{A}$, where $\mathbf{W}_m$ is a diagonal matrix with elements $1/\sqrt{B_r^2 + \epsilon^2}$, where $\epsilon = 10^{-6}$ nT is Ekblom's parameter included for reasons of numerical stability. This procedure effectively implements the L1 norm, as demonstrated by Aster *et al.* (2013), their section 7.3, and by Farquharson & Oldenburg (1998), their eqs (1), (5) and (18) with $p = 1$.

We minimize the cost function eq. (4) by *Iteratively Reweighted Least Squares* using data weights w defined by Tukey's biweight function with tuning constant $c = 4.5$ (Constable 1988; Farquharson & Oldenburg 1998). Starting from a weakly regularized L2 model, both $\mathbf{W}_d$ and $\mathbf{R}$ are updated at each iteration until convergence. The iteration is terminated when the norm of the model change was less than 0.01 per cent of the model norm. Our choice of regularization parameter $\alpha^2 = 3$ nT^{-1} is discussed in the next section. To ensure that the divergence of the magnetic field vector is zero, the sum over all monopole amplitudes has to vanish, $\sum_{k=1}^{K} q_k = 0$; this constraint is handled by the method described in section 4.5 of Kother *et al.* (2015).

In a final step, we transform the point-source representation to a spherical harmonic expansion. Noting that the potential V of eq. (1) can also be described by a spherical harmonic expansion

$$V(r_i, \theta_i, \phi_i) = a\sum_{n=1}^{\infty}\sum_{m=0}^{n}\left(g_n^m\cos m\phi_i + h_n^m\sin m\phi\right)\left(\frac{a}{r_i}\right)^{n+1} \times P_n^m(\cos\theta_i), \tag{5}$$

the Gauss coefficients (g_n^m, h_n^m) are related to the point-source amplitudes q_k by means of (*cf.* eqs 5 and 6 of Kother *et al.* 2015)

$$g_n^m = \sum_{k=1}^{K}\left(\frac{r_k}{a}\right)^{n+2} q_k P_n^m(\cos\theta_k)\cos(m\phi_k) \tag{6a}$$

$$h_n^m = \sum_{k=1}^{K}\left(\frac{r_k}{a}\right)^{n+2} q_k P_n^m(\cos\theta_k)\sin(m\phi_k). \tag{6b}$$

Collecting the Gauss coefficients in the vector $\mathbf{g} = \{g_n^m, h_n^m\}$, this relationship can be written in matrix form as

$$\mathbf{g} = \mathbf{Dm}. \tag{7}$$

We will use the transformation matrix $\mathbf{D}$ in Section 4.2 in our discussion of the formal variances of the spherical harmonic expansion coefficients.

4 RESULTS

4.1 Model residual statistics

For the purpose of testing, we estimated models using different combinations of data sets, including models that are only determined from low-altitude CHAMP data, models that are determined from field and gradient data (using a combination of the data sets described in Sections 2.1 and 2.2), and models that do not make use of EW gradient data. The models were assessed by visual inspection of maps of B_r and F at Earth's surface, by their spatial power spectra, and by their formal model covariances (details are given below in Section 4.2). From these investigations, we concluded that a model determined entirely from magnetic gradient data (i.e. with no direct use of magnetic field data) using a regularization parameter $\alpha^2 = 3$ nT^{-1} gave the most promising result. In the following, we will concentrate on that model, which we refer to as LCS-1.

Table 1 lists the number of data points, together with means and root-mean-squared (rms) misfit values. The mean and rms values are calculated from the model residuals $\mathbf{e} = \mathbf{d} - \mathbf{d}_{\rm mod}$ using the robust Tukey weights w obtained in the final iteration. Rms misfits of the nightside non-polar scalar gradient data are impressive: 0.14 nT for the NS gradient of all three satellites, and 0.27 nT for the EW gradient data. The dayside rms misfits are slightly higher (0.31–0.34 nT for the NS gradient) due to enhanced ionospheric contributions. As expected, the rms misfit is also higher in the polar regions: 1.37 nT for *Swarm* and 1.50 nT for CHAMP for the along-track gradient $\delta F_{\rm NS}$, and 0.93 nT for the EW gradient $\delta F_{\rm EW}$. The rms misfit of the (non-polar) vector gradient data is slightly

Table 1. Number N of data points, (Tukey-weighted) mean and rms misfit (in nT) of NS scalar (δF_{NS}) and vector ($\delta B_{r,\mathrm{NS}}$, $\delta B_{\theta,\mathrm{NS}}$, $\delta B_{\phi,\mathrm{NS}}$) gradient data, and of EW scalar (δF_{EW}) and vector ($\delta B_{r,\mathrm{EW}}$, $\delta B_{\theta,\mathrm{EW}}$, $\delta B_{\phi,\mathrm{EW}}$) gradient data, at polar ($>\pm 55°$) and non-polar ($<\pm 55°$) QD latitudes and for dark (sun at least 10° below horizon) and sunlit conditions.

	CHAMP			*Swarm* Alpha			*Swarm* Charlie			*Swarm* Alpha–Charlie		
	N	mean	rms	N	mean	rms	N	mean	rms	N	mean	rms
$\delta F_{\mathrm{NS,\,polar}}$	491767	−0.03	1.50	283355	−0.04	1.38	283430	−0.05	1.37			
$\delta F_{\mathrm{NS,non\text{-}polar,dark}}$	691933	−0.01	0.13	416965	−0.00	0.14	417455	−0.00	0.14			
$\delta B_{r,\,\mathrm{NS,\,dark}}$	469839	0.00	0.29	261843	−0.00	0.22	262195	−0.00	0.23			
$\delta B_{\theta,\,\mathrm{NS,\,dark}}$	469839	−0.00	0.31	261843	−0.00	0.24	262195	−0.00	0.25			
$\delta B_{\phi,\,\mathrm{NS,\,dark}}$	469839	−0.00	0.36	261843	−0.00	0.29	262195	−0.00	0.30			
$\delta F_{\mathrm{NS,non\text{-}polar,sunlit}}$	759368	0.01	0.34	456084	0.01	0.31	455305	0.01	0.31			
$\delta F_{\mathrm{EW,\,polar}}$										279628	−0.20	0.93
$\delta F_{\mathrm{EW,non\text{-}polar,dark}}$										414730	−0.07	0.27
$\delta B_{r,\,\mathrm{EW,\,dark}}$										259111	−0.00	0.42
$\delta B_{\theta,\,\mathrm{EW,\,dark}}$										259111	0.00	0.44
$\delta B_{\phi,\,\mathrm{EW,\,dark}}$										259111	0.01	0.57

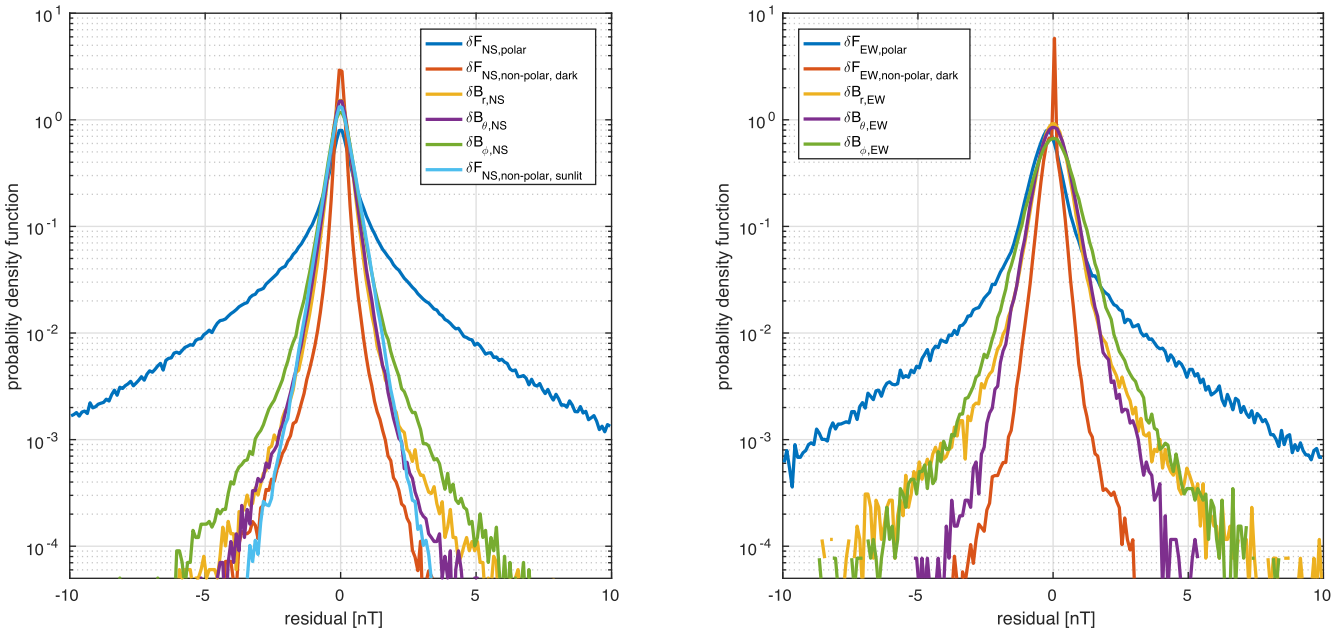

Figure 4. Estimated pdfs of gradient data residuals to LCS-1 for the various data sources listed in Table 1, for NS gradient (left) and EW gradient (right) data.

higher compared to scalar gradient data, varying between 0.23 and 0.36 nT for the NS gradient and between 0.42 and 0.57 nT for the EW gradient.

These numbers refer to the data that have been used to construct the final LCS-1 model. The weighted rms difference between LCS-1 model predictions and magnetic field values (*cf.* Section 2.2) that have *not* been used in model determination is about 4.5 nT for the scalar field in polar regions and 1.4–2.8 nT for the vector components at non-polar latitudes.

All these numbers demonstrate the high quality and consistency of the satellite data, and thereby also of the lithospheric model derived from these data.

Fig. 4 shows estimated probability density functions (pdfs) of model residuals for the various data sources listed in Table 1 (pdfs are very similar for the three satellites and therefore the presented pdfs refer to the combined data sets). These pdfs demonstrate long-tailed distributions for all the data types justifying the use of a robust method to minimize the influence of outliers. The scatter of the residuals is largest for the polar data (blue curves) and smallest for the low-latitude scalar data (red curves), in agreement with the numbers in Table 1.

4.2 On the contribution of *Swarm* constellation data

The LCS-1 model includes, in addition to along-track (NS) gradient data from the CHAMP satellite, NS and EW gradient data as provided by the *Swarm* satellite constellation. However, the *Swarm* spacecraft are presently at much higher altitude (450 km) than CHAMP during its final years (<350 km), and *Swarm* therefore measures a much weaker lithospheric signal than CHAMP. The question therefore arises how much do the *Swarm* satellite data contribute to the combined model, and whether or not they improve on a CHAMP-only model given the higher altitude of *Swarm*.

In order to investigate this, we construct the model covariance matrix $\mathbf{C}_m$ for models determined using different data set combinations. The diagonal elements of $\mathbf{C}_m$ contain the variances σ_m^2 of the model parameters and enable an assessment of the relative

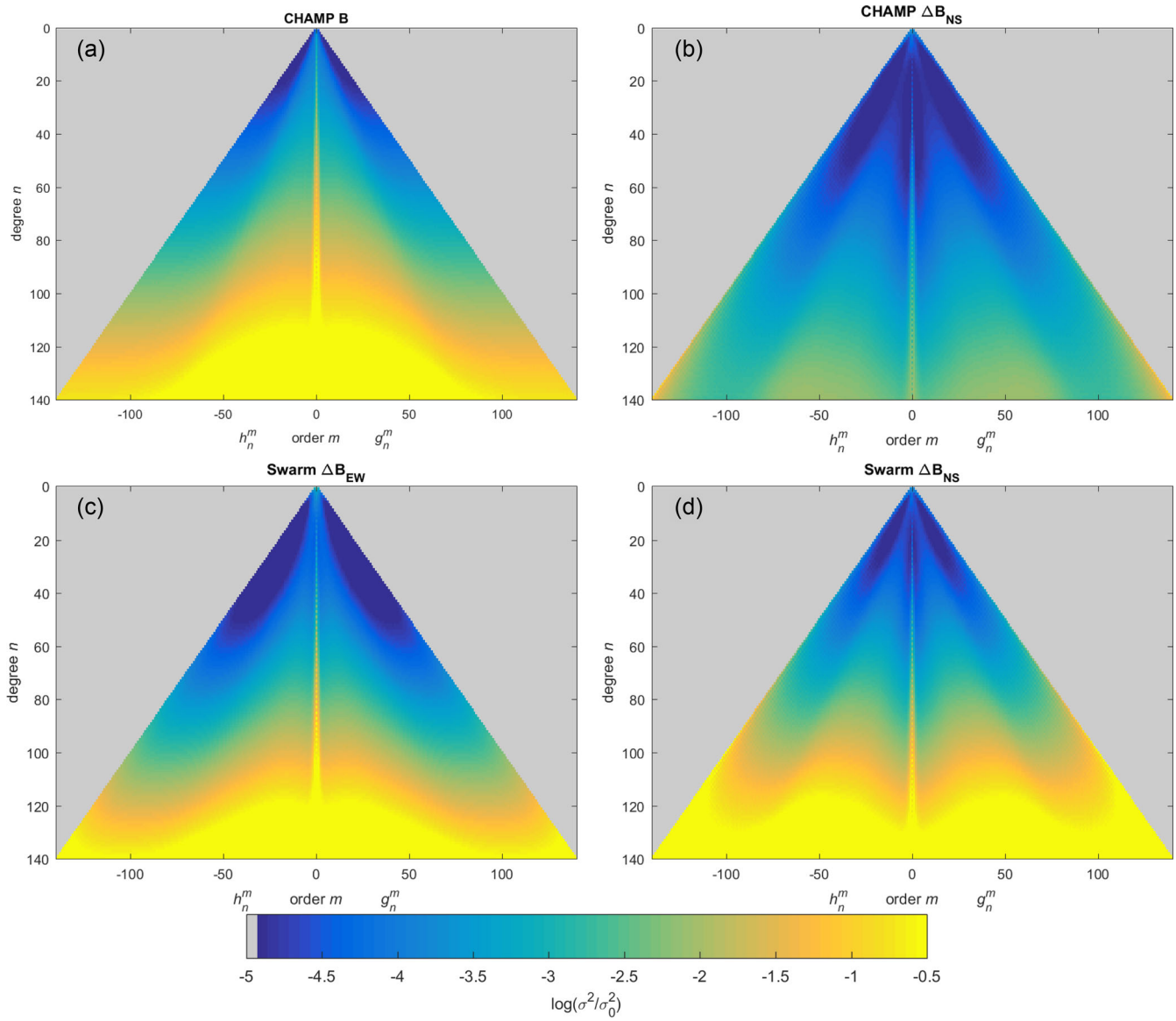

Figure 5. Variance of the spherical harmonic expansion coefficients g_n^m, h_n^m for various input data sets. See the text for details. Blue corresponds to well-resolved coefficients (i.e. low variance), while yellow corresponds to poorly resolved coefficients (i.e. large variance).

contributions from the various data sets. A similar approach has been used by Olsen *et al.* (2010) to assess the relative performance of different satellite constellation concepts for geomagnetic field modeling.

The model covariance matrix, in the absence of regularization ($\alpha^2 = 0$), is given by

$$\mathbf{C}_m = \left(\mathbf{G}^T \mathbf{W}_d \mathbf{G}\right)^{-1}. \tag{8}$$

To construct this matrix, no actual data are used; the matrix is entirely calculated from the positions of the data points, the assigned data uncertainties and the data type (field or gradient data). However, in our case $\mathbf{C}_m$ depends indirectly on the data through the robust data weights w which depend on the data residuals $\mathbf{e}$, that is, on data minus model predictions.

Eq. (8) describes the covariances of the estimated point-source amplitudes q_k. In order to compare models determined from different data sets, it is more convenient to look at the covariances of the spherical harmonic expansion coefficients $\mathbf{g} = \{g_n^m, h_n^m\}$. Using the inverse of $\mathbf{D}$ from eq. (7), the covariances of g_n^m, h_n^m are

$$\mathbf{C}_{g,h} = \left(\left(\mathbf{D}^{-1}\right)^T \mathbf{G}^T \mathbf{W}_d \mathbf{G}\, \mathbf{D}^{-1}\right)^{-1}, \tag{9}$$

and the diagonal elements of $\mathbf{C}_{g,h}$ are the variances $\sigma_{g,h}^2$ of the coefficients g_n^m, h_n^m.

Fig. 5 shows the dependence of $\sigma_{g,h}^2$ on spherical harmonic degree n and order m (shown only up to $n = 140$), with $m \geq 0$ referring to the coefficients g_n^m and $m < 0$ referring to h_n^m. Since the *absolute* values of $\sigma_{g,h}^2$ rely on the assumption of uncorrelated data uncertainties—a condition that might not be fulfilled—we present here only the *relative* value of $\sigma_{g,h}^2$ on an arbitrary scale by dividing with a reference variance (arbitrarily chosen to be $\sigma_0^2 = 1\ \mathrm{nT}^2$) which, however, is the same for all the cases presented in the figure. Blue colours show low variances, while yellow represent larger variances.

Fig. 5(a) shows the variances $\sigma_{g,h}^2$ for a model that is based on CHAMP scalar and vector field (but no gradient) data, while

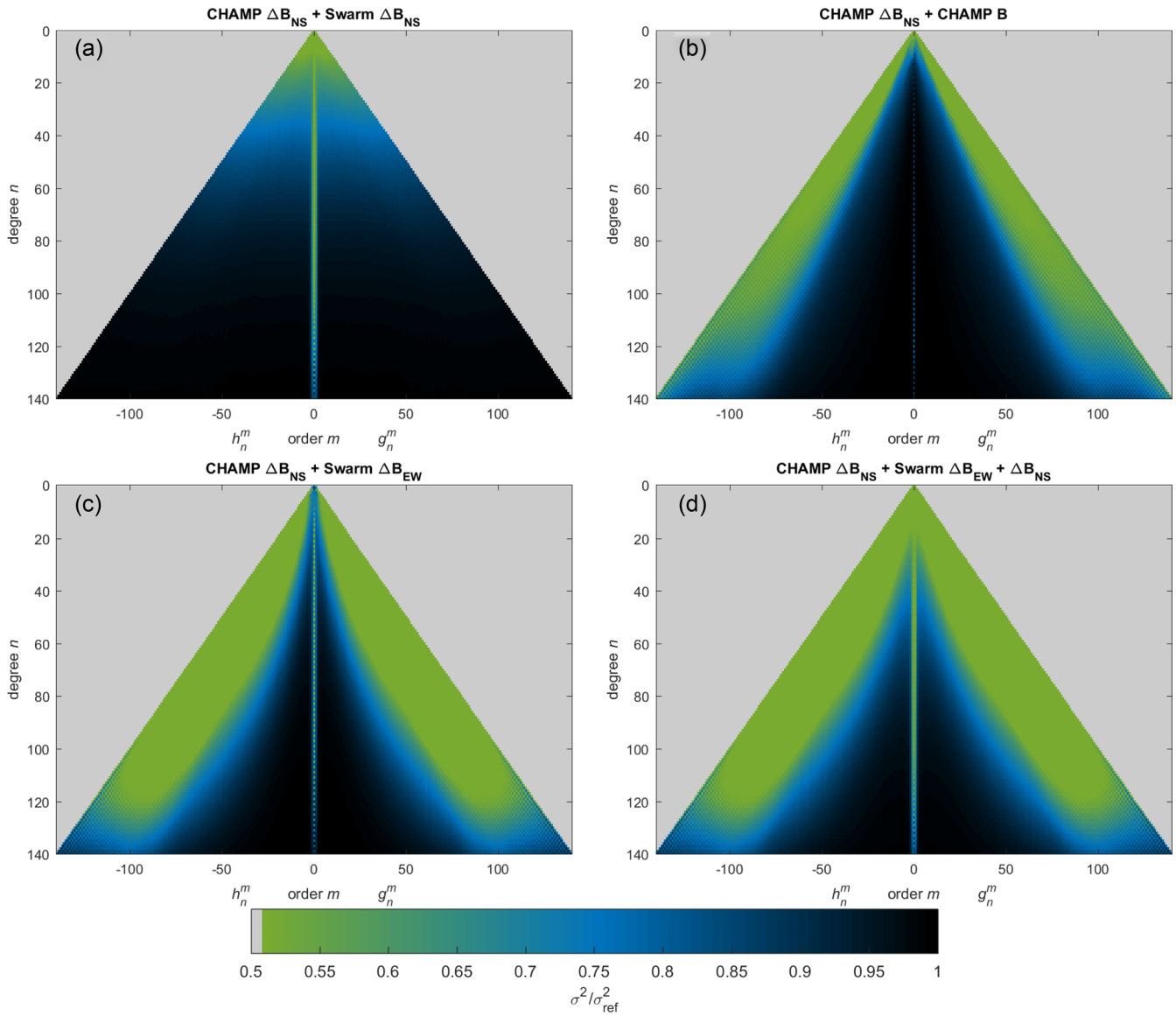

Figure 6. Variance ratio for models estimated from combined CHAMP + *Swarm* data sets, compared to the CHAMP-only model of Fig. 5b). Green corresponds to potential model improvement (i.e. reduction of variance), while black corresponds to no improvement.

Fig. 5(b) presents variances for a model that uses CHAMP scalar and vector NS gradient (but no field) data. NS gradient data improve the determination in particular of spherical harmonic terms of degree n larger than approximately 100 as can be seen from the reduced variance of those coefficients. NS gradient data are, however, not able to improve high-degree near-sectoral coefficients (i.e. coefficients with order $m \approx n$).

The variances shown in Fig. 5(b) are representative of what can be achieved with single-satellite NS gradient data taken at altitudes of 350 km and below. The corresponding results for the *Swarm* satellite mission when both lower spacecraft are treated as single satellites (i.e. no use of EW gradient data) is shown in Fig. 5(d); the variances are considerably larger, in particular for higher degrees n, due to the higher altitude of the *Swarm* satellites.

However, taking advantage of the unique constellation aspect of *Swarm*, we estimated coefficient variances from a data set that only consists of *Swarm* EW gradient data (i.e. no use of NS gradient data). The results, presented in Fig. 5(c), are similar as those obtained with *Swarm* NS gradient data (Fig. 5d) and CHAMP field data (Fig. 5a).

From these results, it is obvious that the low-altitude CHAMP NS gradient data set is the single data set which provides most information on the lithospheric field. We therefore will use the CHAMP gradient-only model of Fig. 5(b) as reference in an investigation of the *incremental* value of adding other data sets in addition to the CHAMP NS gradient data.

Fig. 6 shows the ratio of the coefficient variances of different data set combinations, divided by the variances of the CHAMP gradient-only solution (which is now taken as the reference model). A value of that ratio close to 1 (presented by black) indicates no improvement, whereas values below 1 (green and blue) represent a potential model improvement.

Results for a model that is based on CHAMP and *Swarm* NS gradient data (but neither field nor *Swarm* EW gradient data) are shown in Fig. 6(a): the variance ratio is close to 1 for most of the coefficients, indicating only marginal improvement of the combined model compared to the CHAMP-only reference solution (Fig. 5b). Exceptions are low-degree coefficients ($n < \approx 40$) and the near-zonal terms (i.e. terms with order $m \approx 0$); they are obviously improved

for all degrees n. The reason for this could be the higher altitude of *Swarm* or the slightly higher orbital inclination of the lower *Swarm* pair (87.4°) compared to CHAMP (87.2°), thereby reducing the 'polar gap' (which is the region around the geographic poles that is left unsampled).

Inclusion of CHAMP field observations (the additional data set described in Section 2.2 with data uncertainties assigned using an approach similar to that used for the gradient data) together with the CHAMP NS gradient data results in an improvement of the near-sectoral terms ($m \approx n$), as can be seen from Fig. 6(b).

However, a similar variance reduction can also be achieved when including *Swarm* EW gradient data instead of the CHAMP field observations, as demonstrated in Fig. 6(c). (Note that the actual model improvement might be even larger than the variance reduction shown in this figure, since gradient data are less affected by remaining external field contamination.)

We finally determined the model improvement when using *Swarm* NS and EW gradient data together with the CHAMP NS gradient data. As expected, this combines the model improvements of Figs 6(a) and (c), resulting in variance ratios shown in Fig. 6(d).

We conclude that combining CHAMP NS and *Swarm* NS and EW gradient data leads to a significant reduction of variances by up to 50 per cent (corresponding to a reduction of the variance ratio from 1 to 0.5) compared to a CHAMP-only model, clearly demonstrating that *Swarm* data can improve lithospheric field models, despite their higher altitude, and without the need to directly include magnetic field observations.

5 DISCUSSION

Maps of the vertical component Z and of the scalar anomaly F at Earth's surface from the LCS-1 model are shown in Fig. 7, synthesized for spherical harmonic degrees $n = 16$–185. The maps show the expected anomaly features throughout the world: the cratonic regions of the continents (Archeans and Proterozoic domains) have stronger anomalies than the accreted Palaeozoic and younger crusts and the long-wavelength features associated with and subparallel to the oceanic magnetic reversal stripes are seen consistently on or near widely separated isochrones (Müller *et al.* 2008), especially near the edges of the Cretaceous quiet zones where the width of the magnetic contrast zones is large (isochrones are shown in Fig. 7 as green curves; similar maps without isochrones can be found in the Supporting Information). For the first time, we can observe from maps prepared from the satellite data alone the EW oceanic features associated with the reversal stripes formed in the last 50 Ma of separation history of Australia from Antarctica. In previous field models, these features have been overwhelmed presumably by along-track noise lending them more NS trending appearance which is not expected based on the alignment of stripes and their offsets across transform faults in this region.

A number of other magnetic features of the ocean crust are seen for the first time. For example, there are NS trending lows in the vertical component map that appear to be associated with the NS trending 85°E ridge in the Bay of Bengal. Near the magnetic equator, NS features do not have distinct anomaly signatures in the intensity anomaly. This characteristic of the 85°E ridge has not previously been recognized as the near-surface magnetic anomaly data are intensity values and the Z-component in MF7 does not show a distinct correlation with the ridge. A second new feature is a linear doublet of NS trending anomalies along the southern segment of the 90°E ridge (between latitudes 15°S and 30°S, where it lies just west of the 90°E longitude). Only the anomaly features associated with the Broken Ridge in the southernmost part of this NS feature were known prior to this study (Krishna *et al.* 2012) as there are few marine profiles in the southern segment of the 90°E ridge.

Another interesting feature is the NS trending anomaly south of the Walvis Ridge within the Cretaceous quiet zone (between latitudes 30°S and 45°S and along approx. 5°E longitude) and not parallel to the nearby edge of the Cretaceous quiet zone. Available marine magnetic grids (e.g. EMAG3 and EMAG2_V3 models) show data in the region but in the tracks available to us there are many gaps as well. Since the LCS-1 model has more uniform data coverage in the region, we believe this feature is real and could be associated with coalescence of magnetic anomalies (Taylor & Ravat 1995) leading to linear trends (Ravat 2011) from processes such as later magmatic intrusions, variable magma supply, variable Fe content, variable magnetic thickness, geomagnetic excursions and variability of the palaeomagnetic field (Granot *et al.* 2012).

The EMM2015 lithospheric field model developed by Maus and co-workers (www.ngdc.noaa.gov/geomag/EMM/) and the WDMAM2 model (Lesur *et al.* 2016), truncated to degree 185, also show features cross-cutting the central South Atlantic isochrones. This region has very few marine magnetic tracks, similar to the southern oceans regions away from continental margins. In LCS-1, these cross-cutting features are significantly subdued.

On the continents, where there are aeromagnetic data in EMM2015 and WDMAM2, the features in LCS-1 (in both Z and F, Fig. 7) are similar to those models truncated at degree 185. The importance of LCS-1 is most apparent where the aeromagnetic or near-surface data do not exist or are sparse. The detail in the Bangui anomaly region, as well as several other regions of Africa, has improved substantially in comparison to the truncated EMM2015 or WDMAM2 models. The boundaries of features in the Bangui regions are better defined in LCS-1 Z-component anomalies. Similarly, the Kenya and Ethiopian domes are locations where NS features are expected because of the geology of the East African Rift, but such features could not be identified in previous maps. In the LCS-1 Z-component map (Fig. 7, top), we now observe a distinct alignment of positive features skirting east of Lake Victoria and also an alignment of negative features on the western flank of the Ethiopian dome (42°E and 8°–14°N). Not all sources of the lows can be related to the rift or to flood basalts (White & McKenzie 1989; Hofmann *et al.* 1997) which needs to be investigated further in detail.

The lithospheric power is higher in continental regions compared to oceanic regions, as expected due to the generally thicker continental/cratonic crust. The global average of B_r^2 at Earth's surface is 48.5 nT^2 (for spherical harmonic degrees $n = 16$–185), the power in continental regions is 66.1 nT^2, while that of the oceanic regions is only 39.4 nT^2. Use of L1 model regularization (i.e. minimizing the global average of $|B_r|$ at the surface) helps in achieving this difference between continents and oceans; a L2-regularized model (i.e. constructed to minimise the global average of B_r^2) that has the same *global* power (48.5 nT^2) as the L1 model has a smaller continental power (63.6 nT^2) and higher oceanic power (40.1 nT^2) than the L1-regularized model. As a result, the L2-regularized model shows more spurious features in oceanic regions than the L1-regularized model with the same global power; avoiding spurious oceanic features using L2-regularization requires heavier damping which results in reduced global power. This illustrates a key advantage of L1-regularization for deriving global models that involve both high- (e.g. continental) and low-amplitude (e.g. oceanic) regions.

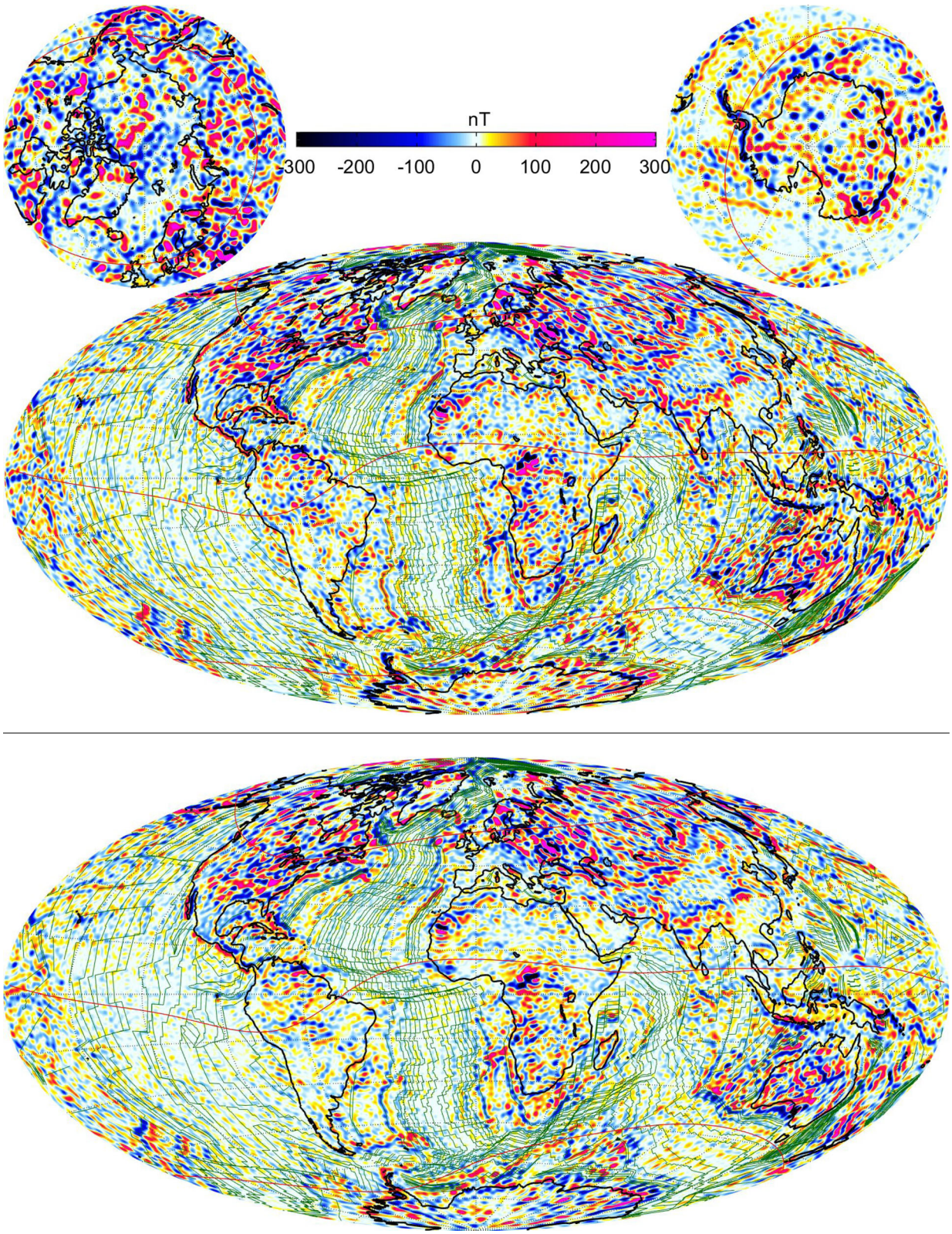

Figure 7. Maps of the lithospheric field vertical component Z (top) and of scalar anomaly F (bottom) at Earth's surface (ellipsoid) from the LCS-1 model, for spherical harmonic degrees $n = 16$–185. Red curves represent QD latitudes of $\pm 55°$, respectively 0°, while green curves show isochrones.

Global *Lowes–Mauersberger* spatial spectra for various lithospheric field models are compared in the top panel of Fig. 8. There is excellent agreement between the various models for spherical harmonic degrees up to, say, $n = 90$ (the power, a quadratic measure, of our L1-regularized model LCS-1 is slightly less than that of the L2-regularized models MF7, CHAOS-6 and EMM2015). For degrees $n = 90$–130, the power of LCS-1 and MF7 is at a similar level, while that of CHAOS-6 is slightly higher (probably

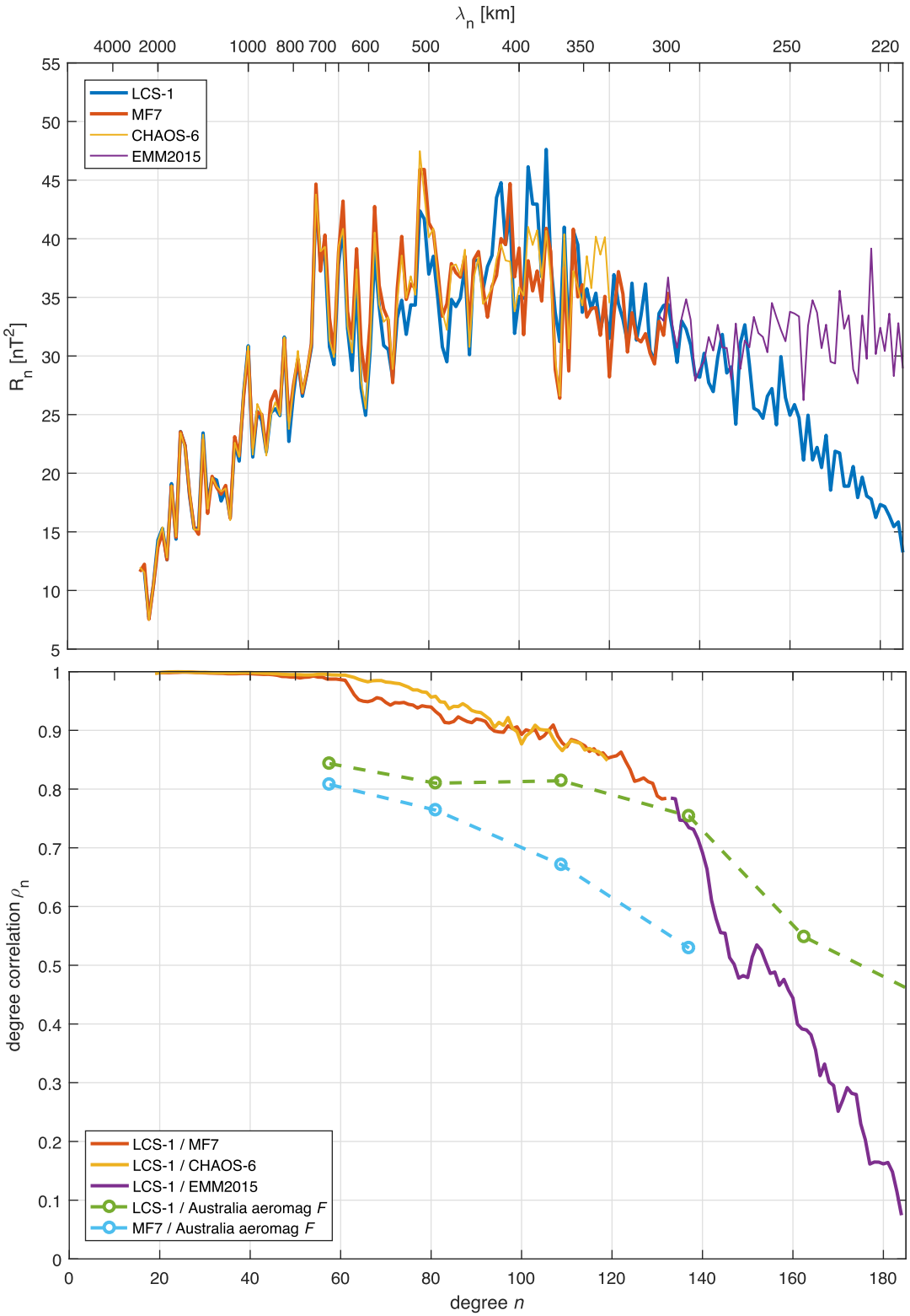

Figure 8. Top panel: spatial power spectrum at Earth's surface for various lithospheric field models in dependence on spherical harmonic degree ρ_n (bottom x-axis), respectively equivalent wavelength λ_n (top axis). Bottom panel: spherical harmonic degree correlation (solid curve). For comparison, the regional coherence (dashed curves) for Australia is also shown (*cf.* Fig. 10).

indicating limitations of CHAOS-6 at higher degrees). The decrease of power in LCS-1 for $n > 130$ is influenced by the regularization. The EMM2015 model is a combination of MF7 (for $n \leq 133$) and the EMAG2_V3 marine/aeromagnetic data sets ($n \geq 133$), formally going up to spherical harmonic degree and order 720. The EMAG2_V3 data set is, however, not of uniform global coverage, and therefore the EMM2015 model, although formally a *global* model, only contains accurate short-wavelength lithospheric field

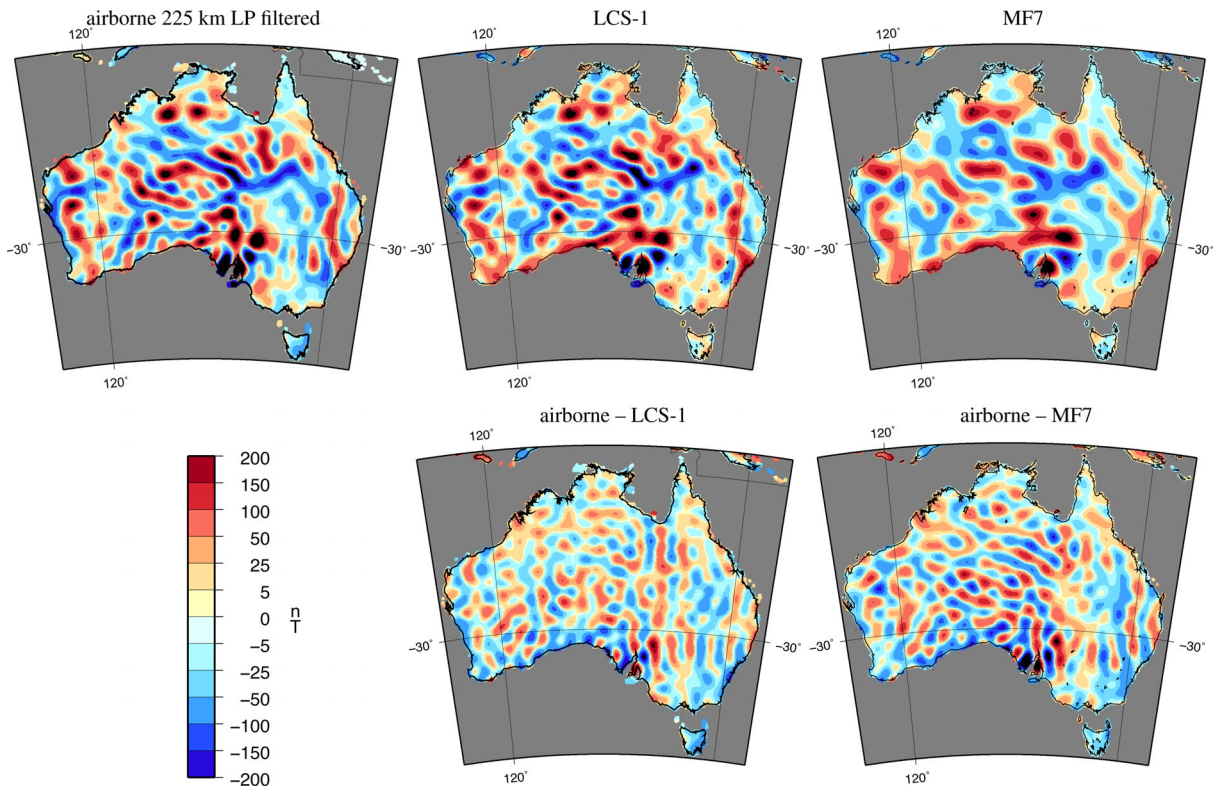

Figure 9. Top: comparison of total intensity magnetic anomalies from LCS-1 and MF7 models with the low-pass filtered (225 km) Australian aeromagnetic data set. Bottom: the difference between this aeromagnetic data set and LCS-1, respectively MF7. In places, the LCS-1 model has spatial resolution approaching 225 km.

features (corresponding to degrees $n > 133$) in regions with sufficient near-surface data coverage. Although EMM2015 shows the highest power of all models at $n > 133$, it is therefore likely that EMM2015 also underestimates the global lithospheric power above degree 133.

The lower panel of Fig. 8 shows the degree correlation ρ_n [see eq. 4.23 of Langel & Hinze (1998) for a definition] between LCS-1 and various other field models. The degree correlation is above 0.9 for all degrees $n \leq 100$ and above 0.8 for all degrees $n \leq 130$. No other satellite-derived global lithospheric models exist for degrees above $n = 133$ and therefore an assessment of the high-degree part of our model is not straightforward. Despite the limitations of EMM2015 in providing a global representation of the lithospheric field for degrees $n > 133$, the degree correlation between LCS-1 and EMM205 for $n = 134$–140 (where EMM2015 is entirely based on near-surface data were available) is above 0.7, which is encouraging.

Next we assess our lithospheric field model using independent near-surface magnetic data. Australia is the only continent with a near-perfect regional aeromagnetic coverage. This coverage was possible due to the backbone of baseline Australia-wide Airborne Geophysical Surveys [AWAGS and AWAGS2 flight lines supplemented with a network of magnetic base stations, Milligan *et al.* (2010)]; thus, this region has excellent long-wavelength control for assessing different global models. We compared the wavelength content of LCS-1, MF7 and EMM2015 models with respect to this Australian data set. Fig. 9 shows a spatial comparison of magnetic field intensity anomalies in the Australian aeromagnetic anomaly grid (filtered with a low-pass wavelength cut-off of 225 km) and the LCS-1 and MF7 models. It is clear that most of the anomaly features in the 225 km filtered data are observable in the LCS-1 field intensity anomalies with nearly the same resolution (except in south-central Australia). MF7 is limited by its truncation at spherical harmonic degree and order of 133.

The visual comparison in Fig. 9 is corroborated by estimates of coherence in the central third of Australia (Fig. 10). For estimating coherence (i.e. the normalized cross-spectrum, see eq. 9.1.36 of Priestley 1981) between two maps we use two identical data windows and 2-D multitapering (Hanssen 1997) to improve statistical properties of the low wavenumbers of the spectra of the signals (since there are only a few estimates of Fourier amplitudes available in the low wavenumbers), and compute annular averages over a band of wavenumbers.

If certain wavelengths are not present in the data sets being compared or the signal at those wavelengths is corrupted or phase-shifted, coherence is reduced. Since the Australian magnetic data are of very high fidelity and full spectrum, based on the degree/order of the spherical harmonic expansion of EMM2015, LCS-1 (considering degrees up to $n = 185$), and MF7 models, we expect their coherence with the Australian aeromagnetic data to degrade around wavelengths of 55, 215 and 300 km, respectively. This is seen to occur as expected at a coherence value of 0.5 in each case. EMM2015 reflects the fact that the model uses the Australian aeromagnetic database for wavelengths less than 300 km. LCS-1 has clearly benefited in terms of resolution by using gradients of the fields from CHAMP and *Swarm* satellites. LCS-1 also has better coherence at the longest wavelengths (900–1500 km) in the central Australian spectral window. Similar analysis has been performed over other Australian regions with similar results. The central Australian region has correlation coefficient of 0.84 and amplitude ratio of 0.86 between the low-pass filtered (at 250 km) aeromagnetic data and the LCS-1 model, whereas MF7 compares to the aeromagnetic data with a correlation coefficient of 0.65 and an amplitude ratio of 0.5.

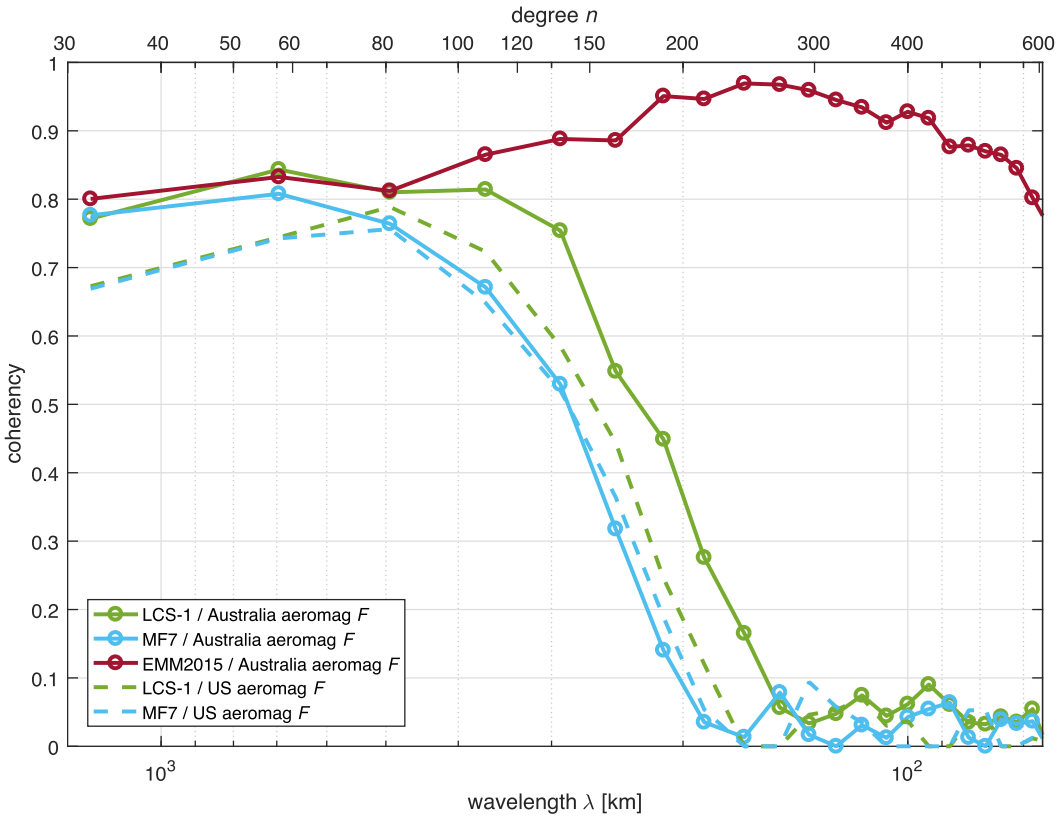

Figure 10. Solid lines: spectral comparison (coherence) between the Australian full spectrum data in the central third of Australia and LCS-1, MF7 and EMM2015 models. The region of comparison is limited by the maximum Cartesian dimension of a study region and hence is limited to 1500 km. All data were projected to Lambert Conical projection and gridded in Cartesian coordinates using identical projection and gridding parameters. Dashed lines: a similar spectral comparison of the models with NURE-NAMAM2008 database in the central U.S. Bottom axis shows horizontal wavelength and top axis shows the equivalent spherical harmonic degree.

A coherence analysis has also been performed over the U.S. where the U.S. NURE aeromagnetic data have been processed using the CM4 continuous core field model (Sabaka *et al.* 2004), instead of IGRF/DGRF, and merged with the North American magnetic anomaly database. The continental U.S. part of the NURE-NAMAM2008 database is full spectrum to the extent that this is possible (Ravat *et al.* 2009) without flying new backbone aeromagnetic surveys as done in Australia. The analysis suggests that the wavelength content of the LCS-1 model is limited to 250 km, while MF7 performs similarly to the central Australian case. EMM2015 on the other hand degrades much more rapidly in North America compared to Australia, reaching coherence of about 0.5 at 85 km wavelength. This is because EMM2015 used Decade of North American Geology magnetic database in the U.S. which has incorrect long wavelengths due to imperfect merging of different aeromagnetic grids and does not take advantage of the intermediate- and long-wavelength corrected NURE-NAMAM2008 database (Ravat *et al.* 2009). Since no other regional compilation in the world has proven high-quality intermediate- and long-wavelength coverage, based on the Australian and the U.S. comparisons, we conclude that the LCS-1 model should improve satellite-based magnetic anomaly definition globally at wavelengths >250 km (i.e. for degrees $n < 160$).

Where can LCS-1 help immediately in magnetic interpretations? Clearly, that would be in regions of the world not presently covered with near-surface magnetic data. This includes large parts of the African continent, regions in South America where data are not publicly available and parts of the southern oceans without adequate magnetic ship tracks. In Fig. 11, we show 3-D surface plots of the field intensity magnetic anomaly over one of the highest amplitude magnetic features on the Earth, the Bangui anomaly in central Africa. The associated high–low–high pattern of anomalies has been interpreted by various researchers since the days of the POGO and Magsat satellites: as magnetic contrast between a large crustal-scale intrusive body situated under the Congo basin and the surrounding central African shields (Regan *et al.* 1975); as strongly magnetized thick iron formation as well as differences in magnetic contrasts between the basins and surrounding shields (Ravat 1989; Ravat *et al.* 1992); and as a large circular region magnetized by asteroid impact (Girdler *et al.* 1989, 1992; Ravat *et al.* 2002). The only known near-surface magnetic data in the region are sparse ground data which show central lobes of −1000 to −1400 nT of 0.5°–1° half-wavelength and northern and southern side lobes of +400 to >600 nT of 0.25°–1° half-wavelength (J. Vassal, unpublished data, 1978, in Regan *et al.* 1975) and hence the high-resolution satellite anomaly models are extremely valuable in the assessment of the origin of geological sources and economic resources of the region. The LCS-1 field intensity anomaly (three narrow and 300–400 nT positive peaks and a few narrow 300–500 nT negative troughs, Fig. 11b) shows significant improvement in spatial resolution over the MF7 field (fewer broader and lower amplitude positive and negative peaks, Fig. 11a). A similar improvement is also seen in the features of west African cratons and the intervening Taoudeni basin in the NW section of the surface plots [for geology and preliminary magnetic crustal models, see Ravat (1989), and references therein].

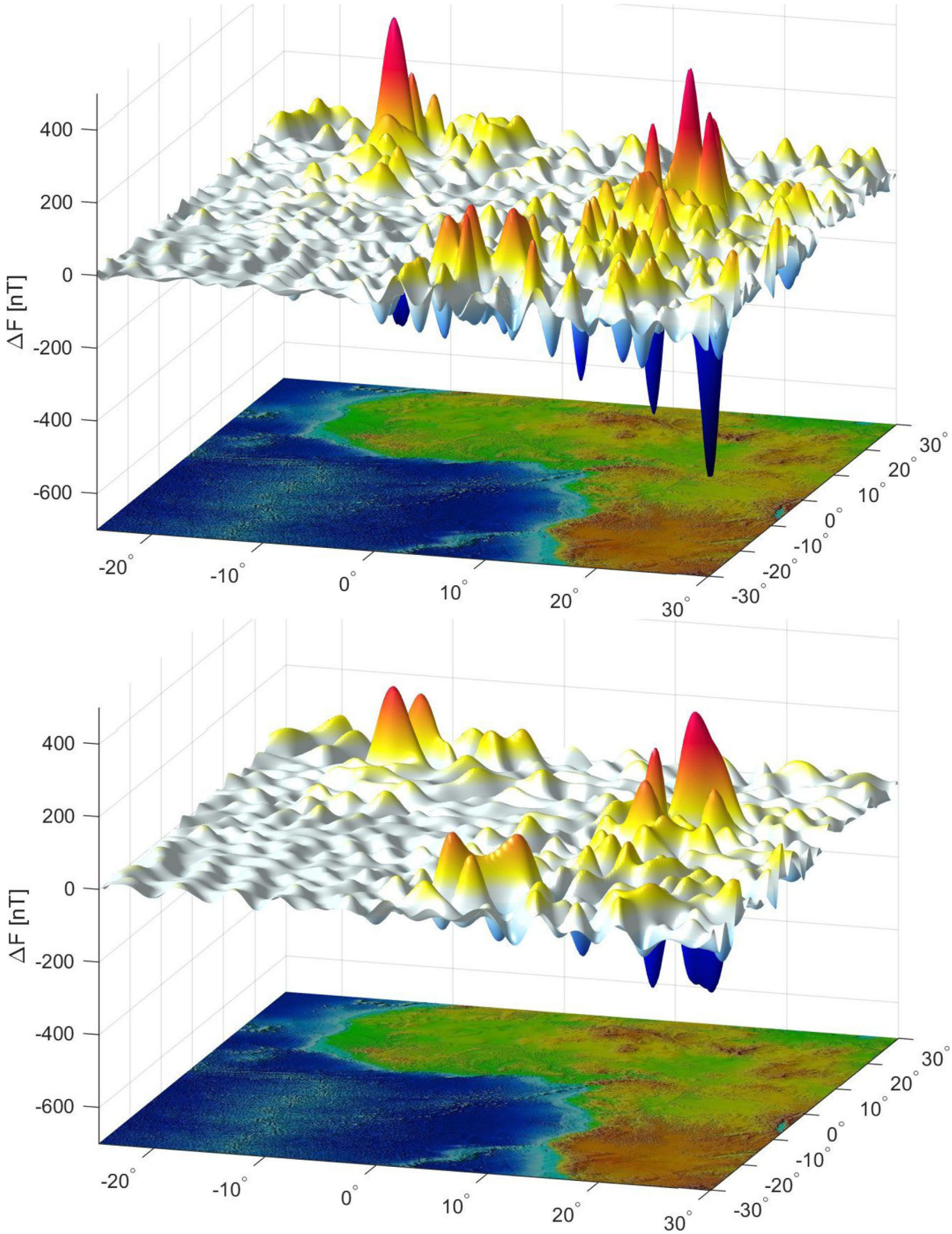

Figure 11. Scalar field anomaly close to Bangui in West-Africa as given by the LCS-1 model (top) and the MF7 model (bottom).

6 SUMMARY AND CONCLUSIONS

We have used four years of CHAMP satellite and three years of *Swarm* satellite constellation magnetic 'gradient' observations (approximated by spatial finite differences of magnetic field observations) to derive a global model of Earth's lithospheric field. The model is regularized by minimizing the L1 norm of the radial magnetic field, $|B_r|$, averaged over Earth's surface.

The resulting model shows very good agreement with other satellite-derived lithospheric field models (degree correlation above 0.8 for all degrees $n \leq 133$). Comparison with independent

near-surface aeromagnetic data from Australia yields good agreement (coherence >0.55) at horizontal wavelengths down to 250 km (corresponding to spherical harmonic degree $n = 160$). Crucial for achieving this result is the EW 'gradient' information that is provided by the unique *Swarm* constellation, despite its present rather high altitude (of about 450 km for the lower satellites) compared to the altitude of CHAMP (below 350 km) during the last four years of its mission. This is very encouraging for future lithospheric field modeling: including forthcoming *Swarm* data taken at lower altitude will certainly further increase the spatial resolution of satellite-derived lithospheric field models.

ACKNOWLEDGEMENTS

We would like to thank Patrick Alken, Mike Purucker and an anonymous reviewer for their constructive comments on an earlier version of the manuscript. The support of the CHAMP mission by the German Aerospace Center (DLR) and the Federal Ministry of Education and Research is gratefully acknowledged. We would like to thank European Space Agency (ESA) for providing prompt access to the *Swarm* L1b data, and Peter Milligan for making available the Australian aeromagnetic data. DR is grateful for support from NASA grants NNX16AJ99G and NNX16AN51G.

REFERENCES

Aster, R., Borchers, B. & Thurber, C., 2013. *Parameter Estimation and Inverse Problems,* Academic Press.

Constable, C.G., 1988. Parameter estimation in non-Gaussian noise, *Geophys. J. Int.,* **94,** 131–142.

Dyment, J. & Arkani-Hamed, J., 1998. Equivalent source magnetic dipoles revisited, *Geophys. Res. Lett.,* **25**(11), 2003–2006.

Farquharson, C.G. & Oldenburg, D.W., 1998. Non-linear inversion using general measures of data misfit and model structure, *Geophys. J. Int.,* **134,** 213–227.

Finlay, C.C., Olsen, N., Kotsiaros, S., Gillet, N. & Tøffner-Clausen, L., 2016. Recent geomagnetic secular variation from Swarm and ground observatories as estimated in the CHAOS-6 geomagnetic field model, *Earth Planets Space,* **68**(1), doi:10.1186/s40623-016-0486-1.

Friis-Christensen, E., Lühr, H. & Hulot, G., 2006. *Swarm*: a constellation to study the Earth's magnetic field, *Earth Planets Space,* **58,** 351–358.

Girdler, R., Taylor, P. & Frawley, J., 1989. Some new thoughts on Bangui, *EOS, Trans. Am. geophys. Un.,* **70,** 314.

Girdler, R., Taylor, P. & Frawley, J., 1992. A possible impact origin for the Bangui magnetic anomaly (Central Africa), *Tectonophysics,* **212**(1), 45–58.

Granot, R., Dyment, J. & Gallet, Y., 2012. Geomagnetic field variability during the cretaceous normal superchron, *Nat. Geosci.,* **5**(3), 220–223.

Haines, G.V., 1985. Spherical cap analysis, *J. geophys. Res.,* **90,** 2583–2591.

Hanssen, A., 1997. Multidimensional multitaper spectral estimation, *Signal Process.,* **58**(3), 327–332.

Hofmann, C., Courtillot, V., Feraud, G., Rochette, P., Yirgu, G., Ketefo, E. & Pik, R., 1997. Timing of the Ethiopian flood basalt event and implications for plume birth and global change, *Nature,* **389**(6653), 838–841.

Kother, L., Hammer, M.D., Finlay, C.C. & Olsen, N., 2015. An equivalent source method for modelling the global lithospheric magnetic field, *Geophys. J. Int.,* **203**(1), 553–566.

Kotsiaros, S., Finlay, C.C. & Olsen, N., 2015. Use of along-track magnetic field differences in lithospheric field modelling, *Geophys. J. Int.,* **200**(2), 878–887.

Krishna, K.S., Abraham, H., Sager, W.W., Pringle, M.S., Frey, F., Gopala Rao, D. & Levchenko, O.V., 2012. Tectonics of the Ninetyeast Ridge derived from spreading records in adjacent oceanic basins and age constraints of the ridge, *J. geophys. Res.,* **117,** B04101, doi:10.1029/2011JB008805.

Langel, R.A. & Hinze, W.J., 1998. *The Magnetic Field of the Earth's Lithosphere: The Satellite Perspective,* Cambridge Univ. Press.

Langel, R.A. & Whaler, K.A., 1996. Maps of the magnetic anomaly field at Earth's surface from scalar satellite data, *Geophys. Res. Lett.,* **23**(1), 41–44.

Leopardi, P., 2006. A partition of the unit sphere into regions of equal area and small diameter, *Electron. Trans. Numer. Anal.,* **25**(12), 309–327.

Lesur, V., Wardinski, I., Rother, M. & Mandea, M., 2008. GRIMM: the GFZ Reference Internal Magnetic Model based on vector satellite and observatory data, *Geophys. J. Int.,* **173,** 382–394.

Lesur, V., Rother, M., Wardinski, I., Schachtschneider, R., Hamoudi, M. & Chambodut, A., 2015. Parent magnetic field models for the IGRF-12 GFZ-candidates, *Earth Planets Space,* **67,** 87, doi:10.1186/s40623-015-0239-6.

Lesur, V., Hamoudi, M., Choi, Y., Dyment, J. & Thébault, E., 2016. Building the second version of the World Digital Magnetic Anomaly Map (WDMAM), *Earth Planets Space,* **68**(1), 27, doi:10.1186/s40623-016-0404-6.

Maus, S., 2007. CHAMP magnetic mission, in *Encyclopedia of Geomagnetism and Paleomagnetism,* pp. 59–60, eds Gubbins, D. & Herrero-Bervera, E., Springer, Heidelberg.

Maus, S., 2010. *Magnetic field model MF7*. Available at: www.geomag.us/models/MF7.html, last accessed 1 September 2017.

Maus, S., Rother, M., Holme, R., Lühr, H., Olsen, N. & Haak, V., 2002. First scalar magnetic anomaly map from CHAMP satellite indicates weak lithospheric field, *Geophys. Res. Lett.,* **29**(10), 45-1–47-4.

Maus, S. *et al.*, 2008. Resolution of direction of oceanic magnetic lineations by the sixth-generation lithospheric magnetic field model from CHAMP satellite magnetic measurements, *Geochem. Geophys. Geosyst.,* **9,** Q07021, doi:10.1029/2008GC001949.

Mayhew, M., 1979. Inversion of satellite magnetic anomaly data, *J. Geophys.,* **45,** 119–128.

Milligan, P., Franklin, R., Minty, B., Richardson, L. & Percival, P., 2010. Magnetic anomaly map of australia (5th edn), 1:5 000 000 scale (digital data set at geophysical archive data delivery system), *Tech. Rep.*, Geoscience Australia, Canberra.

Morschhauser, A., Lesur, V. & Grott, M., 2014. A spherical harmonic model of the lithospheric magnetic field of Mars, *J. geophys. Res.,* **119**(6), 1162–1188.

Müller, R.D., Sdrolias, M., Gaina, C. & Roest, W.R., 2008. Age, spreading rates, and spreading asymmetry of the world's ocean crust, *Geochem. Geophys. Geosyst.,* **9**(4), Q04006, doi:10.1029/2007GC001743.

O'Brien, M.S. & Parker, R.L., 1994. Regularized geomagnetic field modelling using monopoles, *Geophys. J. Int.,* **118,** 566–578.

Olsen, N., Hulot, G. & Sabaka, T.J., 2010. Measuring the Earth's magnetic field from space: concepts of past, present and future missions, *Space Sci. Rev.,* **155,** 65–93.

Olsen, N., Lühr, H., Finlay, C.C., Sabaka, T.J., Michaelis, I., Rauberg, J. & Tøffner-Clausen, L., 2014. The CHAOS-4 geomagnetic field model, *Geophys. J. Int.,* **197,** 815–827.

Olsen, N. *et al.*, 2015. The Swarm Initial Field Model for the 2014 geomagnetic field, *Geophys. Res. Lett.,* **42**(4), 1092–1098.

Olsen, N., Finlay, C.C., Kotsiaros, S. & Tøffner-Clausen, L., 2016a. A model of Earth's magnetic field derived from two years of Swarm satellite constellation data, *Earth Planets Space,* **68,** 124, doi:10.1186/s40623-016-0488-z.

Olsen, N., Stolle, C., Floberghagen, R., Hulot, G. & Kuvshinov, A., 2016b. Special issue "Swarm science results after 2 years in space", *Earth Planets Space,* **68**(1), 172, doi:10.1186/s40623-016-0546-6.

Priestley, M.B., 1981. *Spectral Analysis and Time Series,* Academic Press.

Ravat, D., 1989. Magsat investigations over the greater African region, *PhD thesis,* Purdue Univ., West Lafayette, IN.

Ravat, D., 2011. Interpretation of Mars southern highlands high amplitude magnetic field with total gradient and fractal source modeling: new insights into the magnetic mystery of Mars, *Icarus,* **214**(2), 400–412.

Ravat, D., Hinze, W. & von Frese, R., 1992. Analysis of Magsat magnetic contrasts across Africa and South America, *Tectonophysics,* **212**(1–2), 59–76.

Ravat, D., Wang, B., Wildermuth, E. & Taylor, P.T., 2002. Gradients in the interpretation of satellite-altitude magnetic data: an example from central Africa, *J. Geodyn.,* **33**(1–2), 131–142.

Ravat, D. *et al.*, 2009. A preliminary full spectrum magnetic anomaly database of the United States with improved long wavelengths for studying continental dynamics, *Open-File Rep., U.S. Geol. Surv.*, **1**, 1258.

Regan, R.D., Cain, J.C. & Davis, W.M., 1975. A global magnetic anomaly map, *J. geophys. Res.,* **80,** 794–802.

Richmond, A.D., 1995. Ionospheric electrodynamics using magnetic Apex coordinates, *J. Geomagn. Geoelectr.,* **47,** 191–212.

Sabaka, T.J., Olsen, N. & Purucker, M.E., 2004. Extending comprehensive models of the Earth's magnetic field with Ørsted and CHAMP data, *Geophys. J. Int.,* **159,** 521–547.

Sabaka, T.J., Olsen, N., Tyler, R.H. & Kuvshinov, A., 2015. CM5, a pre-*Swarm* comprehensive magnetic field model derived from over 12 years of CHAMP, Ørsted, SAC-C and observatory data, *Geophys. J. Int.,* **200,** 1596–1626.

Stockmann, R., Finlay, C. & Jackson, A., 2009. Imaging Earth's crustal magnetic field with satellite data: a regularized spherical triangle tessellation approach, *Geophys. J. Int.,* **179**(2), 929–944.

Taylor, P. & Ravat, D., 1995. An interpretation of the Magsat anomalies of central Europe, *J. appl. Geophys.,* **34**(2), 83–91.

Thébault, E., 2006. Global lithospheric magnetic field modelling by successive regional analysis, *Earth Planets Space,* **58,** 485–495.

Thébault, E., 2008. A proposal for regional modelling at the Earth's surface, R-SCHA2D, *Geophys. J. Int.,* **174**(1), 118–134.

Thébault, E., Vervelidou, F., Lesur, V. & Hamoudi, M., 2012. The satellite along-track analysis in planetary magnetism, *Geophys. J. Int.,* **188,** 891–907.

Thébault, E., Vigneron, P., Langlais, B. & Hulot, G., 2016. A Swarm lithospheric magnetic field model to SH degree 80, *Earth Planets Space,* **68**(1), doi:10.1186/s40623-016-0510-5.

Thébault, E., Lesur, V., Kauristie, K. & Shore, R., 2017. Magnetic field data correction in space for modelling the lithospheric magnetic field, *Space Sci. Rev.,* **206,** 191–223.

Thomson, A.W.P. & Lesur, V., 2007. An improved geomagnetic data selection algorithm for global geomagnetic field modelling, *Geophys. J. Int.,* **169**(3), 951–963.

Thomson, A.W.P., Hamilton, B., Macmillan, S. & Reay, S.J., 2010. A novel weighting method for satellite magnetic data and a new global magnetic field model, *Geophys. J. Int.,* **181,** 250–260.

von Frese, R.R., Hinze, W.J. & Braile, L.W., 1981. Spherical earth gravity and magnetic anomaly analysis by equivalent point source inversion, *Earth Planet. Sci. Lett.,* **53**(1), 69–83.

White, R. & McKenzie, D., 1989. Magmatism at rift zones: the generation of volcanic continental margins and flood basalts, *J. geophys. Res.,* **94**(B6), 7685–7729.

SUPPORTING INFORMATION

Supplementary data are available at *GJI* online.

Map of the lithospheric field vertical component Z at Earth's surface (ellipsoid) from the LCS-1 model, for spherical harmonic degrees $n = 16$–185.

Map of the lithospheric field total field intensity anomaly F at Earth's surface (ellipsoid) from the LCS-1 model, for spherical harmonic degrees $n = 16$–185.

Please note: Oxford University Press is not responsible for the content or functionality of any supporting materials supplied by the authors. Any queries (other than missing material) should be directed to the corresponding author for the paper.